[Geophysical Research Letters]

Supporting Information for

Thermoelastic anomaly of iron carbonitride across the spin transition and implications for planetary cores

Shengxuan Huang[1,†], Xiang Wu[2,*], Stella Chariton[3], Vitali Prakapenka[3], Shan Qin[1], Bin Chen[4,*]

[1]Key Laboratory of Orogenic Belts and Crustal Evolution, MOE, Peking University and School of Earth and Space Sciences, Peking University, Beijing, China

[2]State Key Laboratory of Geological Processes and Mineral Resources, China University of Geosciences, Wuhan, China

[3]Center for Advanced Radiation Sources, University of Chicago, Chicago, IL, USA

[4]Hawai'i Institute of Geophysics and Planetology, University of Hawai'i at Mānoa, Honolulu, HI, USA

Corresponding author: Bin Chen (binchen@hawaii.edu); Xiang Wu (wuxiang@cug.edu.cn)

†Current address: Geodynamics Research Center, Ehime University, Matsuyama, Japan

Contents of this file

Text S1. Discussion on the stability of *h*-type $Fe_7(N_{0.75}C_{0.25})_3$

Combining the present results and the previous data, we plot the phase diagram of $Fe_7(N_{0.75}C_{0.25})_3$ to 120 GPa and 2100 K (Figure 1c). Compared with *ε*-type and *o*-type phases of $Fe_7(N_{0.75}C_{0.25})_3$, the *h*-type phase is stable over a much wider pressure range from 40 GPa to at least 120 GPa. The different coordination environments in *ε*-type and *o*-type structures could cause iron carbonitride to be unstable and promote structural transitions upon compression (Huang et al., 2021). The mutual substitution between N and C slightly changes the sub-lattice geometry of the *h*-type structure (Figure S1) (Huang et al., 2021). Therefore, *h*-type $Fe_7(C,N)_3$ could be stable to megabar pressures, similar to its endmembers.

Text S2. Comparison with previous studies

Compared with our previous results (Huang et al., 2021), the volumes obtained in this study are 0.1~0.5% larger than those obtained in the externally-heated DAC experiment but well consistent with those in the LHDAC experiment.

It is possible that the differences could be due to different pressure standards used in the two studies (Ne in run-1 and Au in the previous EHDAC experiment). We have recalculated the pressure for the previous EHDAC experiment using Ne as the pressure calibrator. There is pressure gradient in the sample chamber under high pressure. In the previous EHDAC experiment, the DAC was rotated during the XRD data collection to acquire more diffraction spots (Huang et al., 2021). Therefore, Au was also scanned even at the sample position. As shown in Figure S4a, the pressures determined from Au are the same for different positions. In contrast, the pressure determined from Ne at the sample position is 0.6 GPa higher than that at the Au position. Overall, the difference in pressure is 0.3~0.7 GPa. This can account for 0.1~0.2% volume difference between the previous data and present results (Figure S5). However, there is still 0.3~0.4% volume difference.

We have compared the XRD profile of this study with that in the previous EHDAC experiment (Figure S4b). The 111-peak position of Ne is almost the same for two patterns. However, the characteristic 121 and 022 peaks of *h*-type $Fe_7(N_{0.75}C_{0.25})_3$ in the present study have smaller momentum transfer (that is larger *d*-spacing) than previous data. This indicates that *h*-type $Fe_7(N_{0.75}C_{0.25})_3$ obtained in the present study has a larger volume than that in our previous EHDAC experiment at similar pressure conditions. On the other hand, the volume of *h*-type $Fe_7(N_{0.75}C_{0.25})_3$ obtained in the previous LHDAC experiment (red squares in Figure S5) is well consistent with the present LHDAC experiments.

A recent study has shown that *h*-type Fe_7C_3 could be non-stoichiometric and exhibits chemical composition variations with carbon contents ranging from ~29.5 at% to ~35 at% (Zhu et al., 2019). The unit-cell volume of *h*-type Fe_7C_3 decreases with increasing carbon content. For instance, its ambient unit-cell volume reduces from 187.4 Å with ~29.5 at% carbon to 186.8 Å with ~31 at% carbon and further to 186.2 Å with ~35 at% carbon.

We have checked the chemical composition of our sample $Fe_7(N_{0.75}C_{0.25})_3$ (Huang et al., 2021). The synthetic sample is basically homogeneous, but there are small variations in chemical compositions of our sample. The total contents of nitrogen and carbon in the $Fe_7(N_{0.75}C_{0.25})_3$ sample range from 29.7 at% to 30.7 at%. Based on the results reported by Zhu et al. (2019), such variations in chemical compositions can result in a ~0.3% volume change.

We further compare the data of unit-cell volume and two axes of *h*-type $Fe_7(N_{0.75}C_{0.25})_3$ acquired in this and our previous studies (Huang et al., 2021). As displayed in Figure S6, the compressional behaviors of both unit-cell volume and two axes are very similar for different experimental runs. And there is only a small shift between the data obtained in LHDAC experiments and EHDAC experiments. Therefore, it is reasonable to propose that the small variations in chemical compositions (< 1 at%) have a slight effect on the compressibility of *h*-type $Fe_7(N_{0.75}C_{0.25})_3$.

Although there are some differences in unit-cell volumes of the *h*-type phase at high pressure, the differences among most of studies including ours are within 1.3% (Figure S5) (Chen et al., 2012; Huang et al., 2021; Minobe et al. 2015; Nakajima et al., 2011; Prescher

et al., 2015). However, the data reported in two studies are anomalously lower (Lai et al., 2018; Liu, Li, & Ikuta, 2016). The unit-cell volume of Fe_7C_3 at ambient pressure in the study of Liu et al. (2016) is 186.1 Å, which is the lowest among all studies. The carbon content in their sample is measured to be 30.5 at%, In contrast, Zhu et al. (2019) show that the *h*-type iron carbide with a unit-cell volume of 186.2 Å has a carbon content of ~35 at%. Thus, it remains uncertain whether the chemical composition of *h*-type iron carbide is well determined in the study of Liu et al. (2016). In addition, the authors have also argued that the selection of pressure standard and PTM and the sample loading arrangement could primarily result in such large discrepancy.

Since *h*-type $Fe_7(N_{0.75}C_{0.25})_3$ can only been synthesized above 40 GPa under high temperature, we have applied different sample loading arrangements to laser-heat the sample effectively under high pressure (Figure S2). In run-1, a piece of ε-type $Fe_7(N_{0.75}C_{0.25})_3$ foil was placed on a KCl plate. Then neon gas was loaded. We find that the sample chamber shrank considerably and Re gasket was in touch with KCl plate after Ne was loaded. It implies that the amount of Ne loaded in run-1 should be much smaller than that in the previous EHDAC experiment. This is supported by the fact that the peak intensity ratio of Ne-111 versus *h*-121 in run-1 is much smaller than that in the EHDAC experiment (Figure S4b). Therefore, the pressure environment inside the sample chamber in run-1 is anticipated to be different from that in previous EHDAC experiment.

To summarize, the small differences in the volumes of *h*-type $Fe_7(N_{0.75}C_{0.25})_3$ between this and our previous studies should be primarily attributed to the small variation in chemical compositions of the sample, and secondarily to different PTMs.

Text S3. Equation of state of *h*-type $Fe_7(N_{0.75}C_{0.25})_3$

The *P*-*V* data at 300 K are fitted to the Birch-Murnaghan (B-M) EoS:

$$P(V) = \frac{3}{2}K_0\left[\left(\frac{V_0}{V}\right)^{\frac{7}{3}} - \left(\frac{V_0}{V}\right)^{\frac{5}{3}}\right] \times \left\{1 + \frac{3}{4}(K_0' - 4)\left[\left(\frac{V_0}{V}\right)^{\frac{2}{3}} - 1\right]\right\} \quad (1)$$

where V_0, K_0, and K_0' are zero-pressure unit-cell volume, bulk modulus, and the first pressure derivative of K_0, respectively.

Having established the room-temperature EoS, we further derive the thermoelastic parameters of *h*-type $Fe_7(N_{0.75}C_{0.25})_3$ by fitting the obtained *P*-*V*-*T* data using the thermal pressure model:

$$P(V,T) = P(V, 300\ \mathrm{K}) + P_{\mathrm{th}}(V,T) \quad (2)$$

where $P(V, T)$, $P(V, 300\ \mathrm{K})$, and $P_{\mathrm{th}}(V, T)$ are the total pressure, pressure at 300 K at a given sample volume, and thermal pressure at a given temperature. $P(V, 300\ \mathrm{K})$ is calculated using the room-temperature EoS parameters. The thermal pressure, $P_{\mathrm{th}}(V, T)$, is obtained with two different approaches: (i) the αK_T model and (ii) the Mie-Grüneisen-Debye (MGD) model.

In the αK_T model, $P_{\mathrm{th}}(V, T)$ is described as:

$$P_{\mathrm{th}}(V,T) = \alpha K_T(T - 300) \quad (3)$$

where α is the thermal expansion coefficient. If the anharmonic and electronic contributions could be neglected, the αK_T value is considered constant above the Debye temperature, indicating a simple relation of $\alpha K_T = \alpha_0 K_0$.

In the MGD model (Jackson and Rigden, 1996), $P_{\mathrm{th}}(V, T)$ is derived by:

$$P_{\mathrm{th}}(V,T) = \frac{\gamma}{V}[E_{th}(V,T) - E_{th}(V, 300\ \mathrm{K})] \quad (4)$$

where $E_{\mathrm{th}}(V, T)$, $E_{\mathrm{th}}(V, 300\ \mathrm{K})$, and γ are the internal energy at high temperature, internal energy at 300 K, and Grüneisen parameter, respectively. The internal energy is defined as:

$$E_{th}(V,T) = 9nRT\left(\frac{T}{\theta}\right)^3 \int_0^{\theta/T} \frac{x^3}{e^x - 1} dx \quad (5)$$

where n, R, and θ represent the number of atoms per formula unit (n = 10 in this study), gas constant, and Debye temperature, respectively. The Grüneisen parameter and Debye temperature are also functions of the volume as:

$$\gamma = \gamma_0\left(\frac{V}{V_0}\right)^q \quad (6)$$

$$\theta = \theta_0 e^{(\gamma_0 - \gamma)/q} \quad (7)$$

where γ_0 and θ_0 are Grüneisen parameter and Debye temperature at ambient conditions, respectively. q is a dimensionless parameter, evaluating the volume dependence of γ.

Text S4. Axial compressibility and thermal expansion of *h*-type $Fe_7(N_{0.75}C_{0.25})_3$

The *a* and *c* axes of *h*-type $Fe_7(N_{0.75}C_{0.25})_3$ at various *P*-*T* conditions are plotted in Figure S9. The cube of the lattice parameters at 300 K could be fitted to the B-M EoS to obtain the linear moduli (*M*) and its pressure-derivative (*M*') (Angel et al., 2014). *M* and *M*' are three times those of the volume-like *K* and *K*' values, respectively. For the LS phase, the fitting yields a_0 = 6.824(6) Å and M_a = 1087(22) GPa, and c_0 = 4.541(6) Å and M_c = 620(13) GPa with *M*' being fixed to 9.6, three times of K_0' (3.2). It is noted that this cannot be applied for the HS phase due to limited experimental data. Instead, we simply apply a linear fitting for the HS phase, giving *a* = 6.756(20) - 0.0038(5)**P* and *c* = 4.435(10) - 0.0034(3)**P*. $M_a > M_c$ indicates that the *a* axis is less compressible than the *c* axis in the LS phase. This is also supported by the observation that the *a*/*c* ratio increases with pressure (Figure S10). The *a*/*c* ratio increases with temperature at 45~55 GPa, whereas it is slightly affected by temperature above 70 GPa. Pressure superimposes temperature in controlling the anisotropy of the axial compressibility above 70 GPa. In addition, the values of the *a*/*c* ratio of *h*-type $Fe_7(N_{0.75}C_{0.25})_3$ are comparable to its two endmembers (Chen et al., 2012; Minobe et al., 2015), implying that the compositional effect plays a slight role in the axial compressibility of the *h*-type solid solution.

The thermal expansion coefficients of a^3 and c^3 are calculated using the following equation:

$$\alpha_i = \frac{x_i^3(P,T) - x_i^3(P,300\ K)}{x_i^3(P,300\ K) \times (T-300)} \quad (8)$$

where *i* represents the *a* or *c* axis.

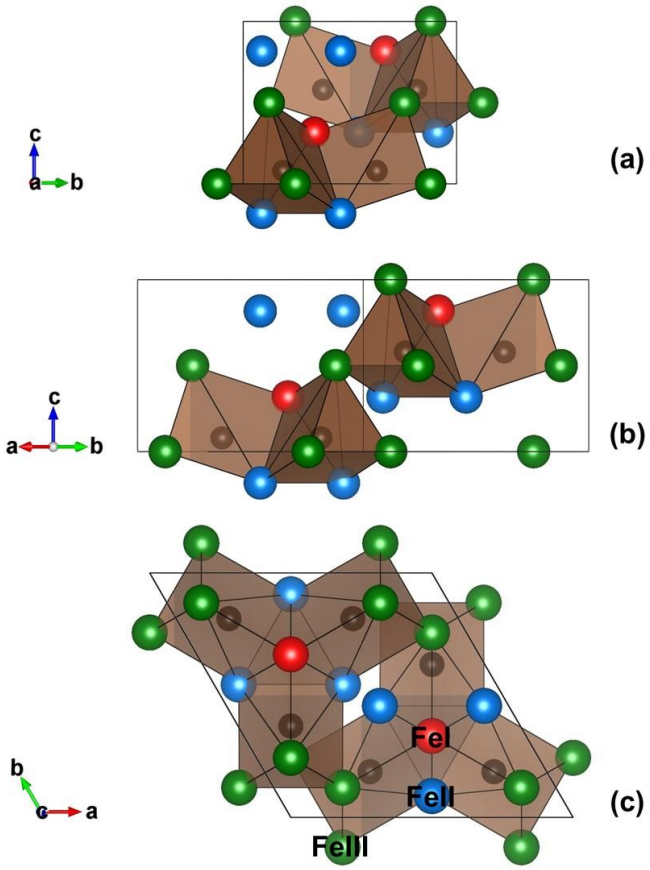

Figure S1. Crystal structure of the *h*-type phase (space group: $P6_3mc$) shown at different orientations. The red, blue and green spheres represent FeI, FeII and FeIII atoms, respectively. C or N atom (black sphere) is surrounded by six Fe atoms (one FeI, two FeII and three FeIII) forming the ditrigonal prism.

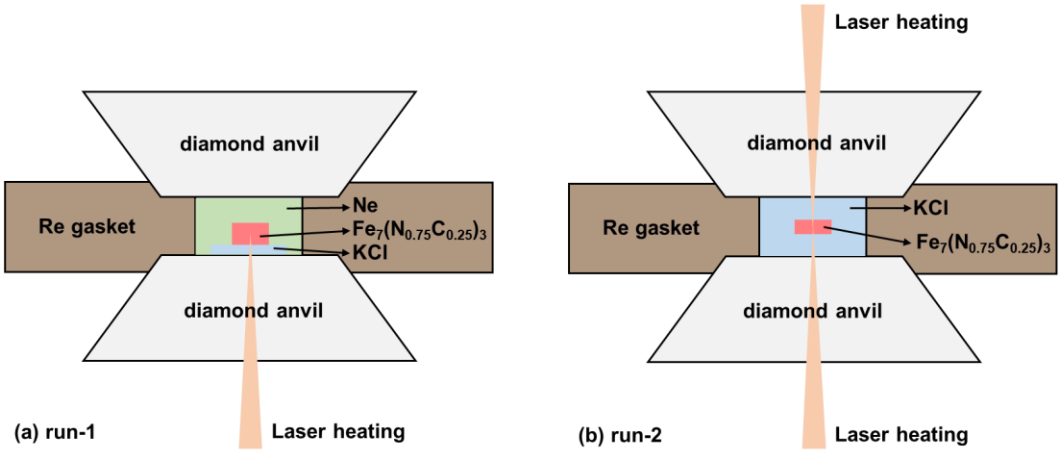

Figure S2 Cross sections of sample configurations used for the LHDAC experiments. (a) for run-1 and (b) for run-2. In run-1, a piece of ε-type $Fe_7(N_{0.75}C_{0.25})_3$ foil was placed on a KCl plate. Then neon gas was loaded. To synthesize the *h*-type phase, we laser-heated the sample from one side at the target pressure. In run-2, the sample was sandwiched between two KCl plates. To synthesize the *h*-type phase, we laser-heated the sample from both sides at the target pressure. We further applied the double-sided laser-heating technique to investigate the phase stability and thermoelastic properties of *h*-type $Fe_7(N_{0.75}C_{0.25})_3$ at simultaneous high-pressure and high-temperature conditions in run-2.

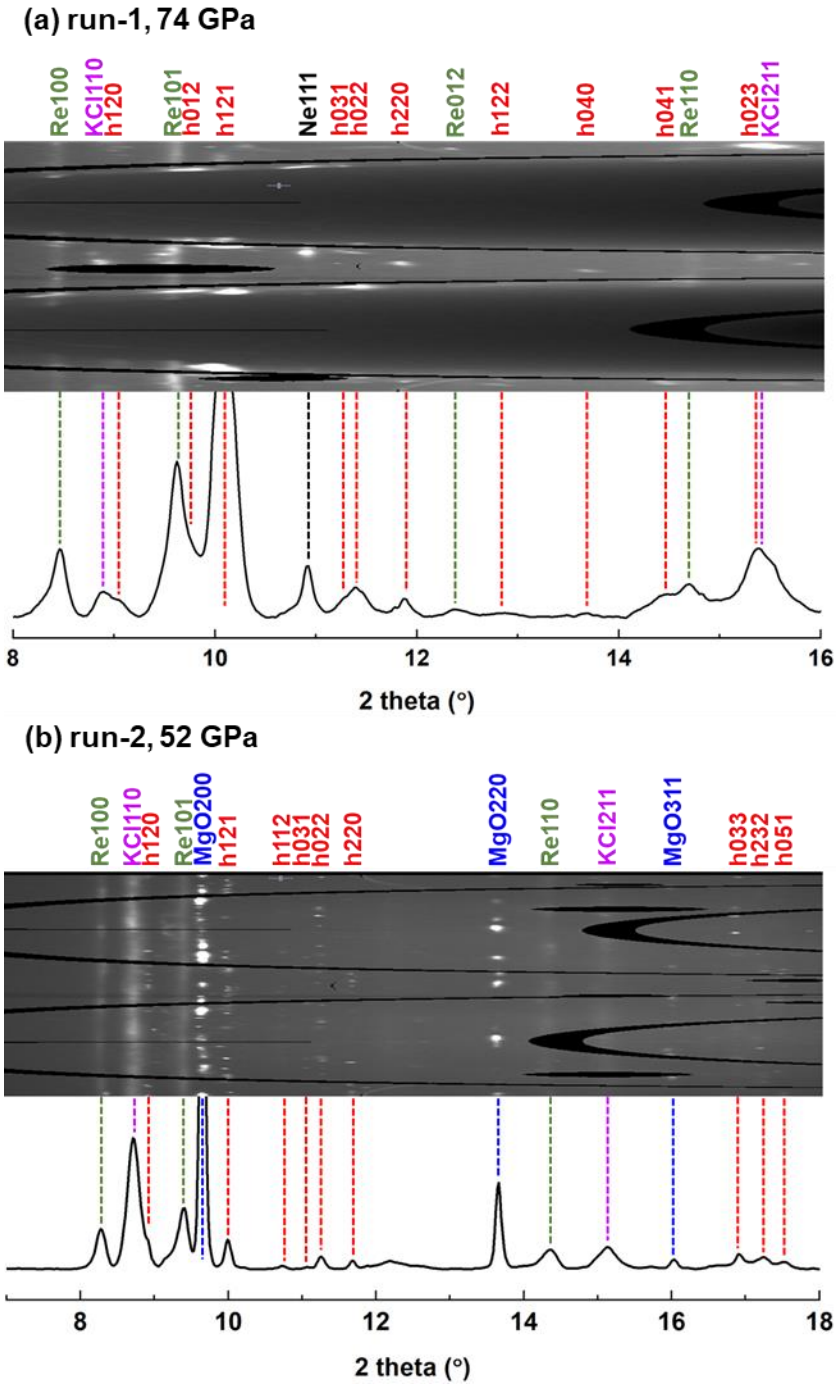

Figure S3 Representative raw data and integrated diffraction patterns of *h*-type $Fe_7(N_{0.75}C_{0.25})_3$ as well as other phases for each run.

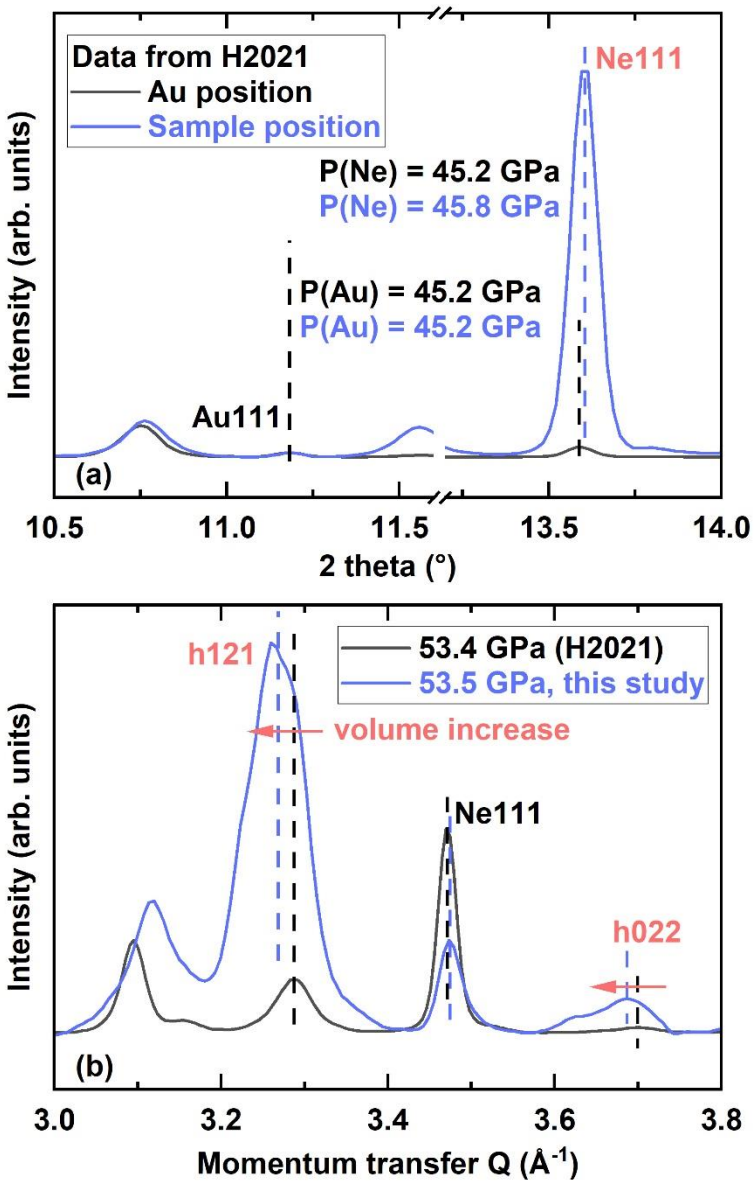

Figure S4 (a) Representative XRD patterns in the EHDAC experiment from Huang et al. (2021). (b) Comparison of the XRD pattern in run-1 with that in the EHDAC experiment from Huang et al. (2021) at similar pressures.

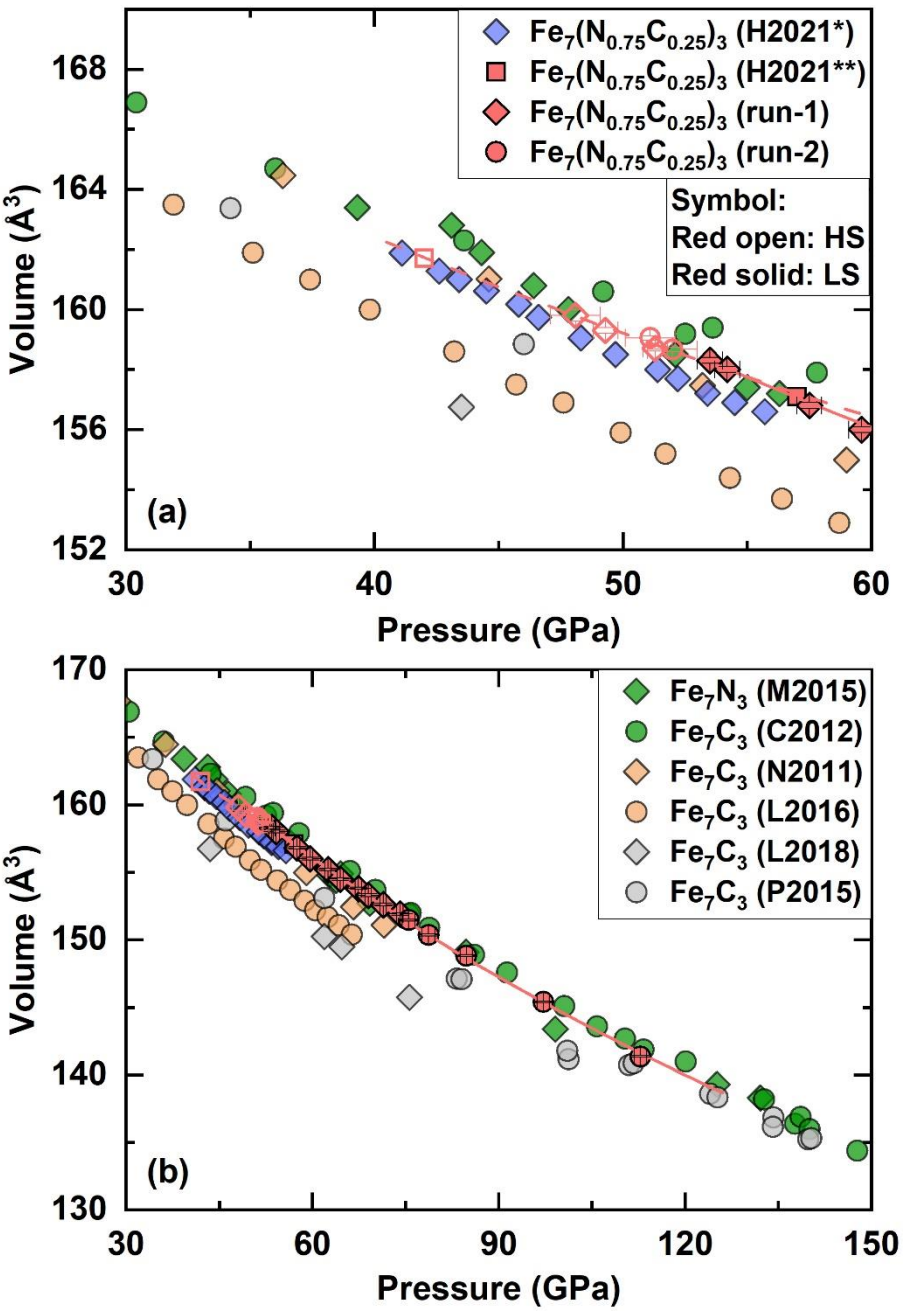

Figure S5 *P*-*V* data of *h*-type $Fe_7(N_{0.75}C_{0.25})_3$ at 300 K. Vertical and horizontal ticks represent error bars for volume and pressure, respectively. The dashed and solid curves are calculated using the B-M EoS parameters of HS- and LS-$Fe_7(N_{0.75}C_{0.25})_3$, respectively. Previous experimental data of $Fe_7(N_{0.75}C_{0.25})_3$, Fe_7C_3 and Fe_7N_3 are plotted for comparison (Chen et al., 2012; Huang et al., 2021; Lai et al., 2018; Liu, Li, & Ikuta, 2016; Minobe et al. 2015; Nakajima et al., 2011; Prescher et al., 2015). "*" and "**" represent EHDAC and LHDAC experimental results in Huang et al. (2021), respectively.

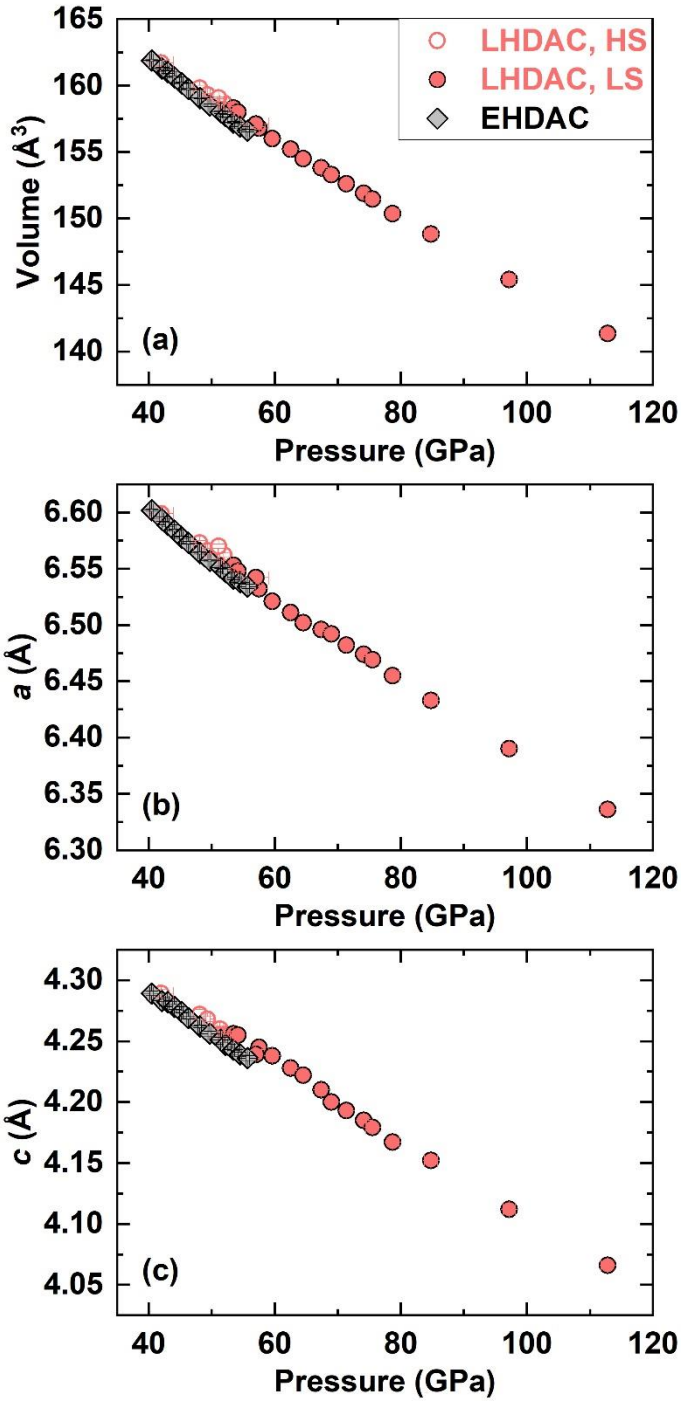

Figure S6 Comparison of the LHDAC data and EHDAC data acquired at 300 K in this study and Huang et al. (2021). (a) *P*-*V*, (b) *P*-*a* axis and (c) *P*-*c* axis.

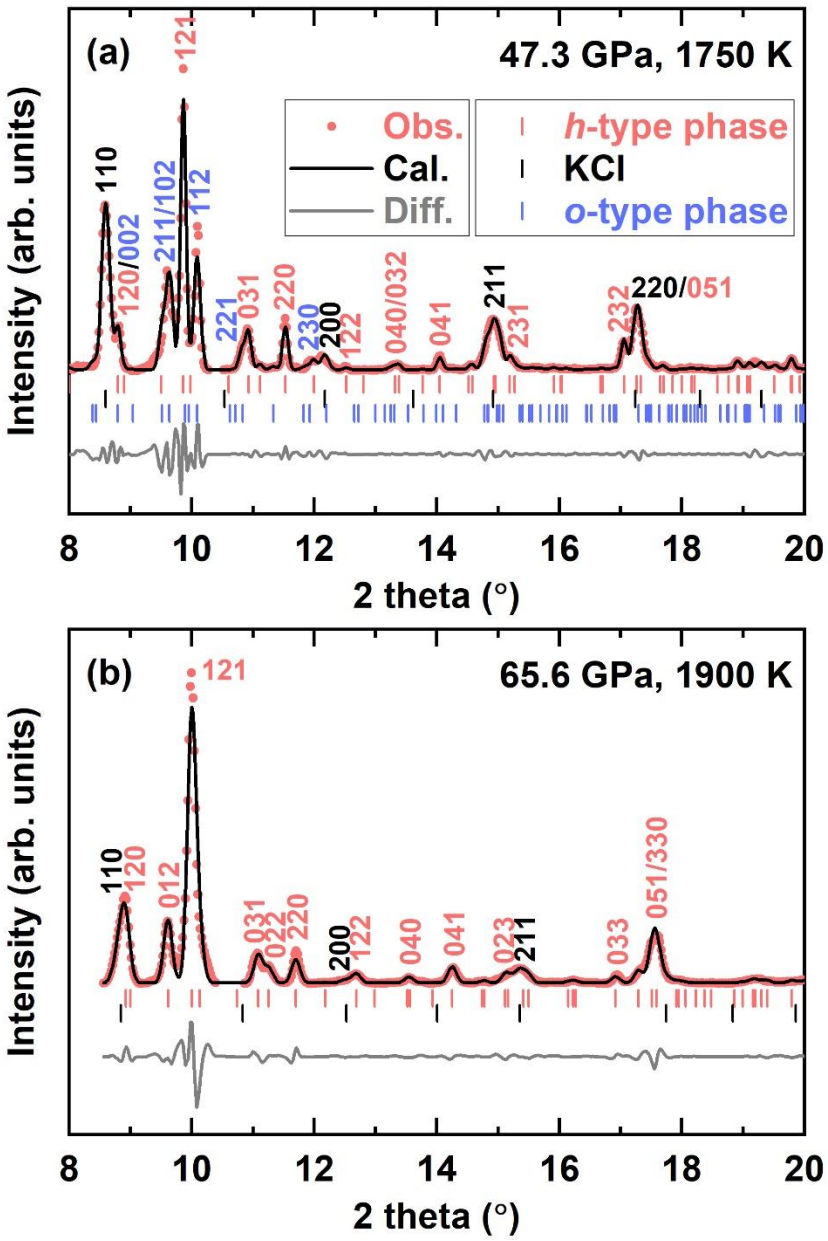

Figure S7 Le Bail fit of XRD spectra of *h*-type $Fe_7(N_{0.75}C_{0.25})_3$ at high pressure-temperature conditions. The XRD data are extracted from previous LHDAC experiments (Huang et al., 2021). Backgrounds are subtracted from the original data. Measured (red circles), calculated (black continuous line) intensities and the difference curve (gray continuous line) between measured and calculated spectra are shown, respectively. The black, red and blue ticks represent Bragg peaks of KCl, *h*-type phase and *o*-type phase, respectively. The pressures under high temperature are re-calibrated based on the thermal equation of state of KCl reported by Chidester et al. (2021).

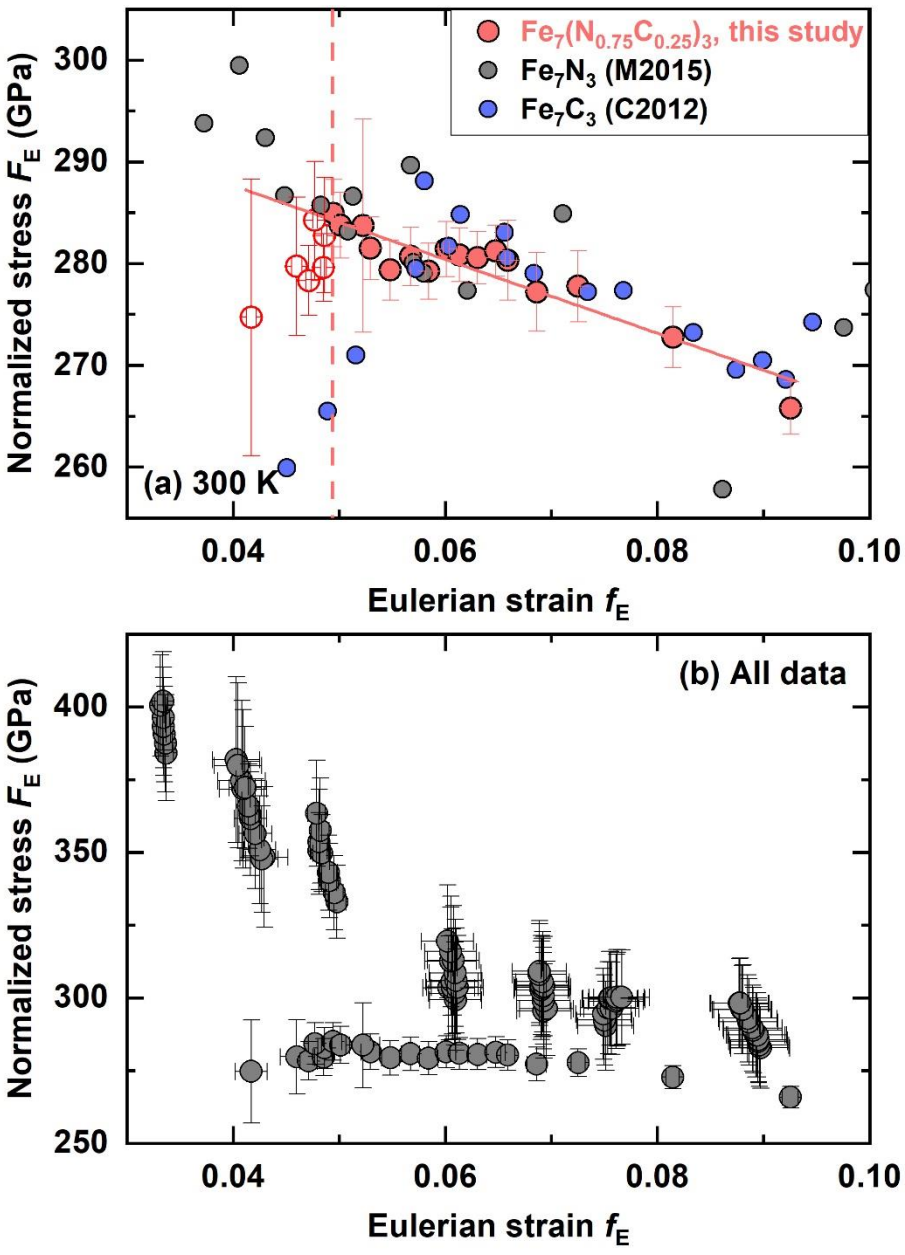

Figure S8 (a) The normalized stress-Eulerian strain (F_E-f_E) plot of the *h*-type phase at 300 K. Previous experimental data of *h*-type Fe_7C_3 and Fe_7N_3 are plotted for comparison (Chen et al., 2012; Minobe et al. 2015). (b) The normalized stress-Eulerian strain (F_E-f_E) plot of the *h*-type $Fe_7(N_{0.75}C_{0.25})_3$ at high *P*-*T* conditions.

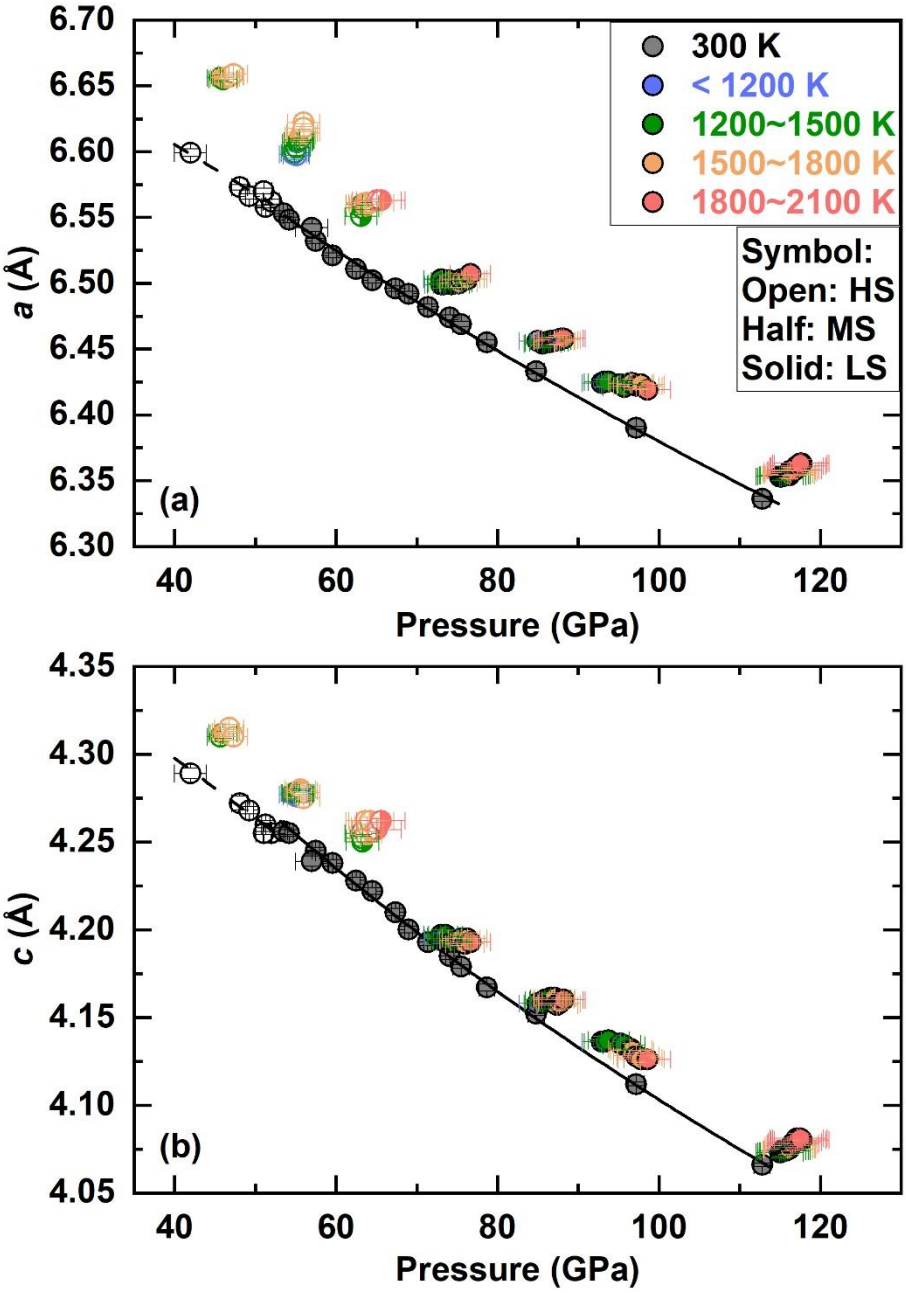

Figure S9 The *a* and *c* axes of *h*-type $Fe_7(N_{0.75}C_{0.25})_3$ at high *P*-*T* conditions. The dashed curves are calculated using linear equations (black open circles). The solid curves are calculated using the B-M EoS parameters (black solid circles). The open, half-solid and solid symbols represent the high-spin (HS), mixed-spin (MS) and low-spin (LS) states, respectively.

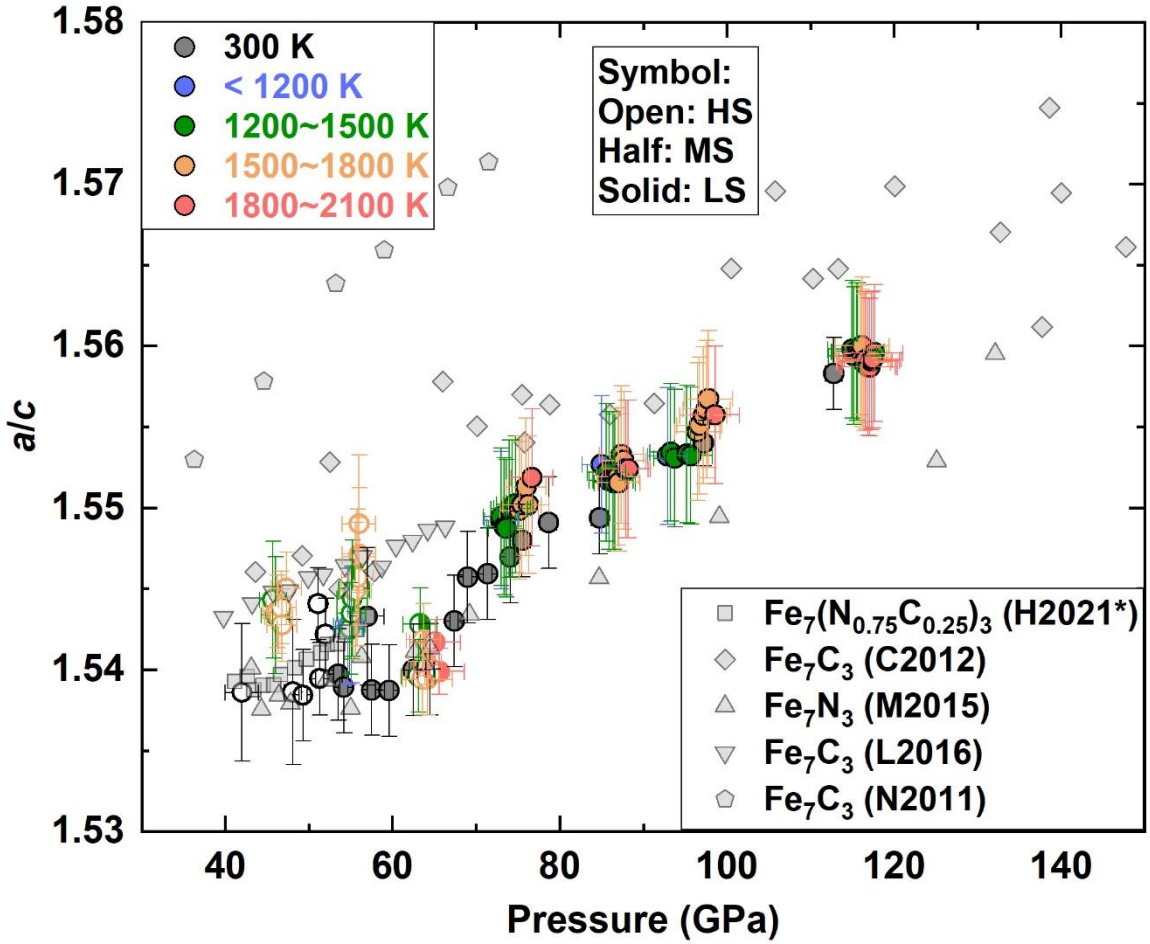

Figure S10 Axial ratio (*a*/*c*) of *h*-type $Fe_7(N_{0.75}C_{0.25})_3$ as a function of pressure. The open, half-solid and solid symbols represent the high-spin (HS), mixed-spin (MS) and low-spin (LS) states, respectively. Previous experimental data of *h*-type $Fe_7(N_{0.75}C_{0.25})_3$, Fe_7C_3 and Fe_7N_3 are plotted for comparison (Chen et al., 2012; Huang et al., 2021; Liu, Li, & Ikuta, 2016; Minobe et al. 2015; Nakajima et al., 2011).

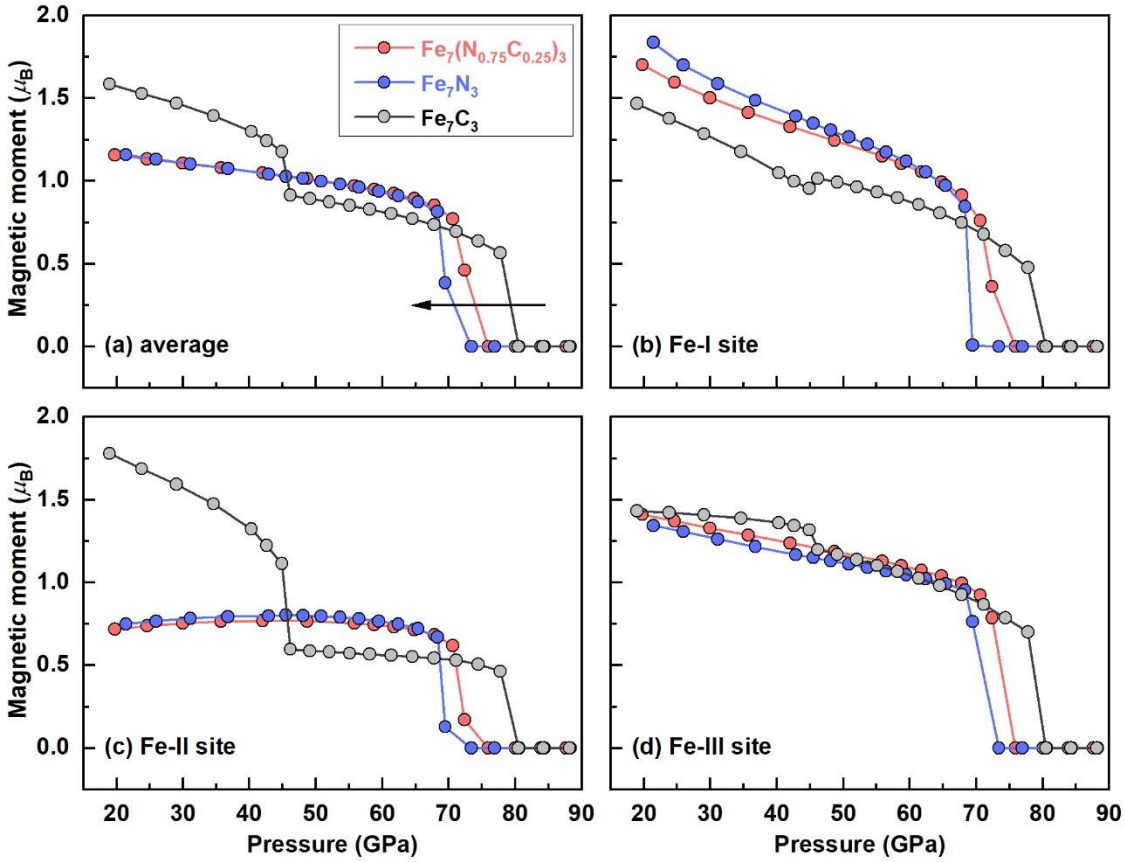

Figure S11 Calculated average magnetic moments (a) and sub-lattice magnetic moments per Fe at each equivalent site (b-d) of *h*-type $Fe_7(N_{0.75}C_{0.25})_3$, Fe_7N_3 and Fe_7C_3 as a function of pressure at 0 K. The black arrow indicates that the substitution of C by N slightly reduces the spin transition pressure of the *h*-type phase.

Table S1. Unit-cell volumes and lattice parameters of *h*-type $Fe_7(N_{0.75}C_{0.25})_3$ at high pressures and room temperature in run-1.

T (K)	*P* (GPa)	*P*_error	*V* (Å^3)	*V*_error	*a* (Å)	*a*_error	*c* (Å)	*c*_error
300	48.1	1.0	159.8	0.2	6.573	0.002	4.272	0.004
300	49.3	0.5	159.3	0.1	6.566	0.002	4.268	0.002
300	51.3	0.5	158.7	0.1	6.558	0.001	4.260	0.002
300	53.5	0.5	158.3	0.1	6.553	0.002	4.256	0.002
300	54.2	0.5	158.0	0.1	6.548	0.002	4.255	0.002
300	57.5	0.5	156.8	0.1	6.532	0.002	4.245	0.002
300	59.6	0.5	156.0	0.1	6.521	0.002	4.238	0.002
300	62.5	0.5	155.2	0.1	6.511	0.002	4.228	0.002
300	64.5	0.5	154.5	0.1	6.502	0.002	4.222	0.002
300	67.4	0.5	153.8	0.1	6.496	0.002	4.210	0.002
300	69.0	0.5	153.3	0.1	6.492	0.002	4.200	0.002
300	71.4	0.5	152.6	0.1	6.482	0.002	4.193	0.002
300	74.1	0.5	151.9	0.1	6.474	0.002	4.185	0.002

Table S2. Unit-cell volumes and lattice parameters of *h*-type $Fe_7(N_{0.75}C_{0.25})_3$ at high-pressure and high-temperature conditions in run-2.

T (K)	*T* error	*P* (GPa)	*P* error	*V* (Å^3)	*V* error	*a* (Å)	*a* error	*c* (Å)	*c* error
300	0	52.0	1.0	158.66	0.07	6.562	0.002	4.255	0.001
1100	110	55.1	1.6	161.16	0.3	6.597	0.003	4.276	0.002
1132	113	54.7	1.7	161.25	0.2	6.598	0.003	4.277	0.002
1204	120	54.9	1.7	161.34	0.2	6.599	0.002	4.278	0.002
1282	128	55.1	1.7	161.53	0.2	6.603	0.002	4.278	0.002
1356	136	55.2	1.8	161.73	0.2	6.607	0.003	4.278	0.002
1384	138	55.4	1.8	161.74	0.1	6.608	0.001	4.277	0.001
1453	145	55.5	1.8	161.82	0.1	6.609	0.001	4.278	0.001
1615	162	55.6	1.9	162.05	0.3	6.612	0.003	4.280	0.003
1651	165	55.8	1.9	162.11	0.3	6.614	0.003	4.279	0.003
1685	169	56.0	2.0	161.96	0.2	6.614	0.002	4.275	0.001
1729	173	56.0	2.0	162.35	0.3	6.622	0.003	4.275	0.003
1760	176	56.0	2.0	162.27	0.3	6.618	0.003	4.278	0.003
300	0	51.1	1.0	159.05	0.07	6.570	0.002	4.255	0.001
1165	117	73.0	2.0	153.45	0.3	6.499	0.003	4.195	0.003
1209	121	73.0	2.1	153.71	0.3	6.503	0.003	4.197	0.003
1236	124	73.4	2.1	153.48	0.3	6.499	0.003	4.196	0.003
1299	130	73.6	2.1	153.57	0.3	6.500	0.003	4.197	0.003
1365	137	74.0	2.2	153.59	0.3	6.502	0.003	4.195	0.003
1402	140	74.3	2.2	153.37	0.3	6.499	0.003	4.193	0.003
1471	147	74.7	2.2	153.42	0.3	6.500	0.003	4.193	0.003
1561	156	75.2	2.3	153.46	0.3	6.500	0.003	4.194	0.003
1631	163	75.5	2.3	153.64	0.3	6.503	0.003	4.195	0.003
1738	174	76.0	2.4	153.53	0.3	6.503	0.003	4.192	0.003
1773	177	76.3	2.4	153.64	0.3	6.503	0.003	4.195	0.003
1848	185	76.7	2.5	153.75	0.3	6.507	0.003	4.193	0.003
300	0	75.5	1.0	151.45	0.07	6.469	0.002	4.179	0.001
300	0	78.7	1.0	150.36	0.1	6.455	0.002	4.167	0.002
1180	118	85.0	2.3	150.09	0.3	6.456	0.003	4.158	0.003
1258	126	85.6	2.3	149.99	0.3	6.454	0.003	4.158	0.003
1325	133	85.9	2.4	150.11	0.3	6.455	0.003	4.160	0.003
1393	139	86.4	2.4	150.11	0.3	6.455	0.003	4.160	0.003

1450	145	86.6	2.5	150.20	0.3	6.456	0.003	4.161	0.003
1532	153	87.0	2.5	150.16	0.3	6.456	0.003	4.160	0.003
1596	160	87.1	2.5	150.20	0.3	6.456	0.003	4.161	0.003
1659	166	87.4	2.6	150.10	0.3	6.457	0.003	4.157	0.003
1742	174	87.7	2.6	150.13	0.3	6.457	0.003	4.158	0.003
1811	181	87.9	2.7	150.25	0.3	6.458	0.003	4.160	0.003
1868	187	88.2	2.7	150.25	0.3	6.458	0.003	4.160	0.003
300	0	84.8	1.0	148.82	0.07	6.433	0.002	4.152	0.001
1175	118	92.9	2.4	147.82	0.3	6.424	0.003	4.136	0.003
1238	124	93.3	2.5	147.86	0.3	6.425	0.003	4.136	0.003
1317	132	93.8	2.5	147.90	0.3	6.425	0.003	4.137	0.003
1380	138	95.2	2.6	147.74	0.3	6.423	0.003	4.135	0.003
1457	146	95.7	2.6	147.61	0.3	6.421	0.003	4.134	0.003
1520	152	96.5	2.7	147.67	0.3	6.424	0.003	4.132	0.003
1590	159	96.7	2.7	147.64	0.3	6.424	0.003	4.131	0.003
1658	166	97.2	2.8	147.44	0.3	6.422	0.003	4.128	0.003
1738	174	97.6	2.8	147.40	0.3	6.422	0.003	4.127	0.003
1792	179	97.8	2.9	147.41	0.3	6.423	0.003	4.126	0.003
1917	192	98.6	2.9	147.23	0.3	6.419	0.003	4.126	0.003
300	0	97.2	1.0	145.41	0.06	6.390	0.001	4.112	0.001
1250	125	115.0	2.9	142.37	0.3	6.353	0.003	4.073	0.003
1343	134	115.2	3.0	142.40	0.3	6.353	0.003	4.074	0.003
1412	141	115.5	3.0	142.45	0.3	6.354	0.003	4.074	0.003
1492	149	115.7	3.1	142.45	0.3	6.354	0.003	4.074	0.003
1576	158	116.0	3.1	142.52	0.3	6.355	0.003	4.075	0.003
1631	163	116.2	3.1	142.48	0.3	6.354	0.003	4.075	0.003
1674	167	116.2	3.2	142.61	0.3	6.357	0.003	4.075	0.003
1741	174	116.4	3.2	142.64	0.3	6.356	0.003	4.077	0.003
1802	180	116.6	3.2	142.76	0.3	6.358	0.003	4.078	0.003
1881	188	116.9	3.3	142.80	0.3	6.358	0.003	4.079	0.003
1977	198	117.1	3.3	143.00	0.3	6.361	0.003	4.081	0.003
2029	203	117.3	3.4	142.97	0.3	6.361	0.003	4.080	0.003
2089	209	117.5	3.4	143.09	0.3	6.363	0.003	4.081	0.003
2086	209	117.7	3.4	143.06	0.3	6.363	0.003	4.080	0.003
300	0	112.8	1.0	141.35	0.07	6.336	0.002	4.066	0.001

Table S3. Summary of thermoelastic parameters of *h*-type $Fe_7(C,N)_3$.

Normalized V_0 (Å^3)*	K_0 (GPa)	K_0'	γ_0	q	θ_0 (K)	α_0 (× 10^{-5} K^{-1})	Ref.
92.35(16)	201(12)	8.0(1.4)	---	---	---	---	PM-Fe_7C_3, Chen et al., 2012**
91.44(38)	307(6)	3.2(1)	---	---	---	---	NM-Fe_7C_3, Chen et al., 2012***
93.1(1)	168(4)	6.1(1)	---	---	---	---	Fe_7C_3, Prescher et al., 2015
92.6(1.0)	246(9)	4 (fixed)	---	---	---	---	Fe_7N_3, Minobe et al., 2015
---	---	---	---	---	---	3.5(6)	PM-Fe_7C_3, Litasov et al., 2015
92.1(3)	253(7)	3.6(2)	2.57(5)	2.2(5)	920(140)	---	PM-Fe_7C_3, Nakajima et al., 2011
93.2(3)	167(4)	5.2(2)	---	---	---	4.7(9)	Fe_7C_3, Lai et al., 2018
90.7(5)	316(5)	3.2 (fixed)	2.1(3)	4.5(9)	430 (fixed)	---	Fe_7N_3, Kusakabe et al., 2019
91.9(2)	201 (fixed)	8.0 (fixed)	2.6(3)	1.0 (fixed)	417 (fixed)	5.4(4)	PM-$Fe_7(N_{0.75}C_{0.25})_3$, this study
91.2(5)	302(7)	3.2 (fixed)	1.3(2)	1.0(4)	417 (fixed)	2.0(2)	NM-$Fe_7(N_{0.75}C_{0.25})_3$, this study

*Normalized V_0 represents volume per formula unit.

**PM represents the paramagnetic state.

***NM represents the nonmagnetic state.

Supplementary references

Angel, R. J., Alvaro, M., & Gonzalez-Platas, J. (2014). EosFit7c and a Fortran module (library) for equation of state calculations. *Zeitschrift für Kristallographie*, 229(5), 405-419. https://doi.org/10.1515/zkri-2013-1711

Chen, B., Gao, L., Lavina, B., Dera, P., Alp, E. E., Zhao, J., & Li, J. (2012). Magneto-elastic coupling in compressed Fe_7C_3 supports carbon in Earth's inner core. *Geophysical Research Letters*, 39(18), L18301. https://doi.org/10.1029/2012GL052875

Chidester, B. A., Thompson, E. C., Fischer, R. A., Heinz, D. L., Prakapenka, V. B., Meng, Y., & Campbell, A. J. (2021). Experimental thermal equation of state of B2-KCl. *Physical Review B*, 104(9), 094107. https://doi.org/10.1103/PhysRevB.104.094107

Huang, S., Wu, X., Zhu, F., Lai, X., Li, J., Neill, O. K., Qin, S., Rapp, R., Zhang, D., Dera, P., Chariton, S., Prakapenka, V. B., & Chen, B. (2021). High-pressure phase stability and thermoelastic properties of iron carbonitrides and nitrogen in the deep Earth. *Journal of Geophysical Research: Solid Earth*, 126(6), e2021JB021934. https://doi.org/10.1029/2021JB021934

Jackson, I., & Rigden, S. M. (1996). Analysis of PVT data: constraints on the thermoelastic properties of high-pressure minerals. *Physics of the Earth and Planetary Interiors*, 96(2-3), 85-112. https://doi.org/10.1016/0031-9201(96)03143-3

Kusakabe, M., Hirose, K., Sinmyo, R., Kuwayama, Y., Ohishi, Y., & Helffrich, G. (2019). Melting curve and equation of state of β-Fe_7N_3: Nitrogen in the core? *Journal of Geophysical Research: Solid Earth*, 124(4), 3448-3457. https://doi.org/10.1029/2018JB015823

Lai, X., Zhu, F., Liu, J., Zhang, D., Hu, Y., Finkelstein, G. J., Dera, P., & Chen, B. (2018). The high-pressure anisotropic thermoelastic properties of a potential inner core carbon-bearing phase, Fe_7C_3, by single-crystal X-ray diffraction. *American Mineralogist*, 103(10), 1568-1574. https://doi.org/10.2138/am-2018-6527

Litasov, K. D., Rashchenko, S. V., Shmakov, A. N., Palyanov, Y. N., & Sokol, A. G. (2015). Thermal expansion of iron carbides, Fe_7C_3 and Fe_3C, at 297-911 K determined by in situ X-ray diffraction. *Journal of Alloys and Compounds*, 628, 102-106. https://doi.org/10.1016/j.jallcom.2014.12.138

Liu, J., Li, J., & Ikuta, D. (2016). Elastic softening in Fe_7C_3 with implications for Earth's deep carbon reservoirs. *Journal of Geophysical Research: Solid Earth*, 121(3), 1514-1524. https://doi.org/10.1002/2015JB012701

Minobe, S., Nakajima, Y., Hirose, K., & Ohishi, Y. (2015). Stability and compressibility of a new iron-nitride β-Fe_7N_3 to core pressures. *Geophysical Research Letters*, 42(13), 5206-5211. https://doi.org/10.1002/2015GL064496

Nakajima, Y., Takahashi, E., Sata, N., Nishihara, Y., Hirose, K., Funakoshi, K. I., & Ohishi, Y. (2011). Thermoelastic property and high-pressure stability of Fe_7C_3: Implication for iron-carbide in the Earth's core. *American Mineralogist*, 96(7), 1158-1165. https://doi.org/10.2138/am.2011.3703

Prescher, C., Dubrovinsky, L., Bykova, E., Kupenko, I., Glazyrin, K., Kantor, A., McCammon, C., Mookherjee, M., Nakajima, Y., Miyajima, N., Sinmyo, R., Cerantola, V., Dubrovinskaia, N., Prakapenka, V., Rüffer, R., Chumakov, A., & Hanfland, M. (2015). High Poisson's ratio of Earth's inner core explained by carbon alloying. *Nature Geoscience*, 8(3), 220-223. https://doi.org/10.1038/ngeo2370

Zhu, F., Li, J., Walker, D., Liu, J., Lai, X., & Zhang, D. (2019). Origin and consequences of non-stoichiometry in iron carbide Fe_7C_3. *American Mineralogist*, 104(3), 325-332. https://doi.org/10.2138/am-2019-6672